Quadrupolar ordering in tetragonal $TmAg_2$

P. Morin and J. Rouchy
Laboratoire Louis Néel, (CNRS) BP 166, 38042 Grenoble CEDEX 9, France
(Received 30 November 1992)

The occurrence of a nonmagnetic transition at 5 K in $TmAg_2$ ($MoSi_2$-type tetragonal symmetry) is analyzed as a ferroquadrupolar ordering within the orthorhombic γ-symmetry-lowering mode. The crystalline-electric-field parameters are obtained by inelastic-neutron-scattering and magnetic-susceptibility measurements. Both the magnetoelastic couplings and the quadrupolar pair interactions are then determined by third-order magnetic-susceptibility, parastriction, and ultrasonic-velocity experiments. The great coherency between these determinations allows us to understand completely the magnetic properties in both the orthorhombic and tetragonal phases. $TmAg_2$ is then an archetype for compounds ruled by quadrupolar interactions.

I. INTRODUCTION

The study of quadrupolar interactions concerning the unfilled $4f$ shell is well developed for rare-earth compounds. It addresses the complex problems of both the crystalline electric field (CEF) acting on a $4f$ ion and the pair interactions between different $4f$ ions.[1] These properties have been extensively studied in many systems exhibiting orbital degeneracy, as reported for cubic spinels such as mixed chromites.[2] The literature concerning rare-earth ions is rich with very complete reviews of the Jahn-Teller effect in rare-earth insulators within the tetragonal zircon structures.[3,4] It demonstrates the relevance of the mean-field approximation to the description of Jahn-Teller orderings such as the paradigm compound $TmVO_4$, as well as to the analysis of the balance between quadrupolar and spin couplings such as $TbPO_4$. A main feature of these systems is that the Jahn-Teller coupling dominates the pair interactions, which are mediated by phonons in these insulators. However, some shortcomings occur in the pseudospin treatment, which neglects the exact mixing of the eigenfunctions by the CEF and therefore the coupling between levels; usually only low-lying levels are considered.

In rare-earth intermetallics, the existence of quadrupolar interactions has been studied only for cubic symmetry.[1] One-ion magnetoelastic couplings have been observed, which lead to record values for the spontaneous magnetostriction [1.7% for the tetragonal symmetry-lowering mode in CeZn (Ref. 5)]. Quadrupolar orderings have also been observed in the paramagnetic state, for instance in cubic TmCd and TmZn. In these standard systems, a close coherency has been found between different determinations of the quadrupolar couplings. This has been facilitated by an exact knowledge of the CEF. The main difference from the rare-earth insulators is that in these intermetallics the pair interactions, mediated by the conduction electrons, dominate the magnetoelastic coupling. It is these interactions that are then responsible for the quadrupolar ordering; if negative, they may drive antiferroquadrupolar orderings as in CeB_6 and $PrPb_3$.[1]

Such thorough studies are made possible by the small number of magnetoelastic and pair-interaction coefficients that are present within the cubic symmetry. Rarer are similar analyses for lower symmetries, such as tetragonal or hexagonal, although the susceptibility treatment, developed in cubic symmetry, has also been established. The literature gives only a few magnetoelastic coefficients in a few hexagonal RCo_5 (Refs. 6 and 1) (R=rare earth) and RNi_5 (Ref. 7) compounds. The RAg_2 series, with tetragonal symmetry, appears to us a favorable case for studying quadrupolar couplings. Indeed, several compounds, $TbAg_2$, $DyAg_2$, $HoAg_2$, and $ErAg_2$, exhibit, immediately below the Néel temperature, complex modulated magnetic structures which transform, through first-order transitions, into commensurate magnetic structures.[8] Magnetoelasticity and, more generally, quadrupolar couplings play an important role in such processes, for instance in cubic $TmGa_3$ or DySb.[1] In addition, $TmAg_2$ has been observed to undergo a second-order transition around 5 K,[9] the nonmagnetic behavior of which was confirmed by the absence of any magnetic reflections in a powder neutron-diffraction experiment.[10] This transition might then be of quadrupolar origin.

We present here an extensive study of the magnetic and magnetoelastic properties of $TmAg_2$. We first briefly recall the relevant Hamiltonian and the susceptibility formalism, which allows us to analyze the magnetic and/or quadrupolar response to external stresses such as a magnetic field and ultrasound waves. We then present the complete determination of the CEF levels and eigenfunctions from inelastic neutron spectroscopy (INS) and magnetic susceptibility measurements. In Sec. V, the analysis of the third-order magnetic susceptibility, the parastriction, and the ultrasonic velocity associated with the different symmetry-lowering modes of the tetragonal cell leads us to conclude that a ferroquadrupolar ordering within a γ-orthorhombic symmetry occurs. In Sec. VI, low-temperature magnetic properties are found to agree with the previous analysis. In conclusion, the coherency of all the results is emphasized, which makes $TmAg_2$ an archetype for such systems ruled by quadrupolar interactions.

0163-1829/93/48(1)/256(13)/$06.00

II. FORMALISM

The magnetic properties of the $4f$ shell are described for a tetragonal symmetry with the following Hamiltonian:[11]

$$\mathcal{H}=\mathcal{H}_{\rm CEF}+\mathcal{H}_Z+\mathcal{H}_B+\mathcal{H}_Q+\mathcal{H}_{\rm ME}+(E_{\rm el}+E_B+E_Q)\ . \tag{1}$$

The CEF term $\mathcal{H}_{\rm CEF}$ is written using the operator equivalent method[12] within a system of x, y, and z axes parallel to the [100], [010], and [001] axes of the body-centered lattice cell, respectively:

$$\mathcal{H}_{\rm CEF}=\alpha_J V_2^0 O_2^0+\beta_J(V_4^0 O_4^0+V_4^4 O_4^4)+\gamma_J(V_6^0 O_6^0+V_6^4 O_6^4)\ . \tag{2}$$

O_l^m are the Stevens operators, V_l^m the CEF parameters, α_J, β_J, γ_J the Stevens coefficients. The $4f$ magnetic moment is coupled through the Zeeman term to the applied magnetic field, $\mathbf{H}$, corrected for demagnetizing effects:

$$\mathcal{H}_Z=-g_J\mu_B\mathbf{H}\cdot\mathbf{J}\ . \tag{3}$$

The bilinear interactions of Heisenberg type are taken into account within the mean-field approximation (MFA):

$$\mathcal{H}_B=-g_J\mu_B n\mathbf{M}\cdot\mathbf{J}\ , \tag{4}$$

with $\mathbf{M}=g_J\mu_B\langle\mathbf{J}\rangle$. $n=\theta^*/C$ is the bilinear exchange coefficient, which may be related to an exchange interaction temperature θ^* through the Curie constant C. The study of $GdAg_2$, where Gd is in an S state, has shown n to be isotropic.[13] Within the MFA, the two-ion quadrupolar term reads

$$\mathcal{H}_Q=-K^\alpha\langle O_2^0\rangle O_2^0-K^\gamma\langle O_2^2\rangle O_2^2-K^\delta\langle P_{xy}\rangle P_{xy}-K^\varepsilon[\langle P_{yz}\rangle P_{yz}+\langle P_{zx}\rangle P_{zx}] \tag{5}$$

with

$$O_2^0=3J_z^2-J(J+1)\ ,$$
$$O_2^2=J_x^2-J_y^2\ ,$$
$$P_{ij}=\tfrac{1}{2}(J_iJ_j+J_jJ_i)\quad(ij=xy,yz,zx)\ .$$

Note that in tetragonal symmetry, the O_2^0 component is already ordered by the CEF, but this does not exclude the possible existence of $\langle O_2^0\rangle$ quadrupolar pair interactions. Only magnetoelastic contributions linear in strain and restricted to second-rank terms are considered here. They read in symmetrized notation[14] as

$$\mathcal{H}_{\rm ME}=-(B^{\alpha1}\varepsilon^{\alpha1}+B^{\alpha2}\varepsilon^{\alpha2})O_2^0-B^\gamma\varepsilon^\gamma O_2^2-B^\delta\varepsilon^\delta P_{xy}-B^\varepsilon(\varepsilon_1^\varepsilon P_{zx}+\varepsilon_2^\varepsilon P_{yz})\ . \tag{6}$$

The strains ε^μ's are given in Table I. The B^μ's are the magnetoelastic coefficients. Note that two-ion magnetoelasticity is usually weak in $4f$ intermetallics[1] and is therefore neglected here. The related elastic energy is written as

$$E_{\rm el}=\tfrac{1}{2}C_0^{\alpha1}(\varepsilon^{\alpha1})^2+C_0^{\alpha12}\varepsilon^{\alpha1}\varepsilon^{\alpha2}+\tfrac{1}{2}C_0^{\alpha2}(\varepsilon^{\alpha2})^2+\tfrac{1}{2}C_0^\gamma(\varepsilon^\gamma)^2+\tfrac{1}{2}C_0^\delta(\varepsilon^\delta)^2+\tfrac{1}{2}C_0^\varepsilon[(\varepsilon_1^\varepsilon)^2+(\varepsilon_2^\varepsilon)^2]\ . \tag{7}$$

The C_0^μ's are the symmetrized background elastic constants in the absence of magnetic interactions (Table I). Corrective energies E_B and E_Q result from the MFA treatment:

$$E_B=\tfrac{1}{2}nM^2\ ,$$
$$E_Q=\tfrac{1}{2}K^\alpha(\langle O_2^0\rangle)^2+\tfrac{1}{2}K^\gamma(\langle O_2^2\rangle)^2+\tfrac{1}{2}K^\delta(\langle P_{xy}\rangle)^2+\tfrac{1}{2}K^\varepsilon(\langle P_{zx}\rangle^2+\langle P_{yz}\rangle^2)\ . \tag{8}$$

Minimizing the free energy with regard to the strains gives the equilibrium strains as functions of the expectation value of the corresponding quadrupolar operators. Replacing these ε^μ's makes $\mathcal{H}_{\rm ME}$ (Eq. 6) undistinguishable from $\mathcal{H}_Q$ [Eq. (5)]:

TABLE I. Symmetrized strains and elastic constants in tetragonal symmetry.

Representations	Strains	Elastic constants
Γ_1	$\varepsilon^{\alpha1}=\frac{1}{\sqrt{3}}(\varepsilon_{xx}+\varepsilon_{yy}+\varepsilon_{zz})$	$C^{\alpha1}=\frac{1}{3}(2C_{11}+2C_{12}+4C_{13}+C_{33})$
Γ_1	$\varepsilon^{\alpha2}=\left[\frac{2}{3}\right]^{1/2}\left[\varepsilon_{zz}-\frac{\varepsilon_{xx}+\varepsilon_{yy}}{2}\right]$	$C^{12}=-\frac{\sqrt{2}}{3}(C_{11}+C_{12}-C_{13}-C_{33})$ $C^{\alpha2}=\frac{1}{3}(C_{11}+C_{12}-4C_{13}+2C_{33})$
Γ_3	$\varepsilon^\gamma=\frac{1}{\sqrt{2}}(\varepsilon_{xx}-\varepsilon_{yy})$	$C^\gamma=C_{11}-C_{12}$
Γ_4	$\varepsilon^\delta=\sqrt{2}\varepsilon_{xy}$	$C^\delta=2C_{66}$
Γ_5	$\varepsilon_1^\varepsilon=\sqrt{2}\varepsilon_{zx}$ $\varepsilon_2^\varepsilon=\sqrt{2}\varepsilon_{yz}$	$C^\varepsilon=2C_{44}$

$$\mathcal{H}_Q+\mathcal{H}_{\rm ME}=-G^\alpha\langle O_2^0\rangle O_2^0-G^\gamma\langle O_2^2\rangle O_2^2-G^\delta\langle P_{xy}\rangle P_{xy}-G^\varepsilon[\langle P_{zx}\rangle P_{zx}+\langle P_{yz}\rangle P_{yz}] \quad (9)$$

with

$$G^\alpha=\frac{(B^{\alpha1})^2C_0^{\alpha2}-2B^{\alpha1}B^{\alpha2}C_0^{\alpha12}+(B^{\alpha2})^2C_0^{\alpha1}}{C_0^{\alpha1}C_0^{\alpha2}-(C_0^{\alpha12})^2}+K^\alpha , \quad (10)$$

$$G^\gamma=\frac{(B\gamma)^2}{C_0^\gamma}+K^\gamma , \quad (11)$$

$$G^\delta=\frac{(B^\delta)^2}{C_0^\delta}+K^\delta , \quad (12)$$

$$G^\varepsilon=\frac{(B^\varepsilon)^2}{C_0^\varepsilon}+K^\varepsilon . \quad (13)$$

In the ordered phases or in the presence of large external stresses, the Hamiltonian has to be self-consistently diagonalized with regard to the three magnetic components and the five quadrupolar ones. However, perturbation theory can be applied very fruitfully to the *disordered phase*. It is then possible to obtain analytical expressions of the free energy associated with each of the symmetry-lowering modes and then to describe the corresponding couplings. Calculations are extensively described in Ref. 11. The magnetization induced by a magnetic field along the [001], [100], and [110] directions may be expanded as

$$M=\chi_M H+\chi_M^{(3)}H^3+\cdots , \quad (14)$$

with

$$\chi_M=\frac{\chi_0}{1-n\chi_0} , \quad (15)$$

$$\chi_M^{(3)}=\frac{1}{(1-n\chi_0)^4}\left[\chi_0^{(3)}+\frac{2G^\alpha(\chi_\alpha^{(2)})^2}{1-G^\alpha\chi_\alpha}+\frac{2G^\mu(\chi_\mu^{(2)})^2}{1-G^\mu\chi_\mu}\right] . \quad (16)$$

The modes $\mu=\gamma,\delta$ are absent for H along [001]. The mode ε, which is weak in $TmAg_2$, will be not considered in the following.

χ_M is the usual (first-order) magnetic susceptibility; χ_0 is the single-ion susceptibility, which is anisotropic between the [001] axis and the basal plane. The third-order magnetic susceptibility $\chi_M^{(3)}$ describes the initial curvature of the magnetization curve and depends on four single-ion susceptibilities: $\chi_0^{(3)}$ describes the curvature of the magnetic response in the absence of any magnetic interaction. It is anisotropic between the [100], [110], and [001] directions. The strain susceptibility, $\chi_\mu=\partial\langle O_2^\mu\rangle/\partial\varepsilon^\mu$ characterizes the response of the Q_μ quadrupolar component to the associated strain; $\chi_\mu^{(2)}=\partial\langle O_2^\mu\rangle/\partial H^2$ is the equivalent in the presence of a magnetic field. The χ_μ's and $\chi_\mu^{(2)}$'s are anisotropic, because they concern different quadrupolar components. The single-ion susceptibilities are deduced immediately from the CEF levels and eigenfunctions (see expressions in Appendix A of Ref. 11. Typical temperature dependences are also given in Ref. 11). These susceptibilities have to be renormalized by possible quadrupolar interactions. From an experimental point of view, the α mode is present alone for H parallel to the [001] axis, the γ and δ modes are active for H along the [100] and [110] directions, respectively.

The strain induced in the disordered phase by a magnetic field is given by

$$\varepsilon^\mu=\frac{B^\mu}{C_0^\mu}\chi_Q^\mu H^2 \quad (17)$$

with

$$\chi_Q^\mu=\frac{\chi_\mu^{(2)}}{(1-n\chi_0)^2(1-G^\mu\chi_\mu)} . \quad (18)$$

This expression includes the renormalization of the applied field by the bilinear interactions, and of the quadrupolar response by the quadrupolar pair interactions. For a magnetic field applied along a $(\alpha_1\alpha_2\alpha_3)$ direction, the change of length measured in the $(\beta_1\beta_2\beta_3)$ direction is given by

$$\lambda_{\alpha_1\alpha_2\alpha_3}^{\beta_1\beta_2\beta_3}=\left[\frac{\delta l}{l}\right]_{\alpha_1\alpha_2\alpha_3}^{\beta_1\beta_2\beta_3}=\frac{\varepsilon^{\alpha1}}{\sqrt{3}}+\frac{1}{\sqrt{6}}\varepsilon^{\alpha2}(2\beta_3^2-\beta_1^2-\beta_2^2)+\frac{1}{\sqrt{2}}\varepsilon^\gamma(\beta_1^2-\beta_2^2)+\sqrt{2}\varepsilon^\delta\beta_1\beta_2+\sqrt{2}\beta_3(\varepsilon_1^\varepsilon\beta_1+\varepsilon_2^\varepsilon\beta_2) . \quad (19)$$

Thus different sets of experimental configurations allows us to study separately the α, γ, and δ modes and to determine the corresponding magnetoelastic and pair interaction coefficients. For instance, the linearized experimental temperature variation leads to B^γ and G^γ by comparison with the variation of $1/(\chi_\gamma^{(2)})^{1/2}$:[11,15]

$$\frac{H}{|\lambda_{100}^{100}-\lambda_{100}^{010}|^{1/2}}=\left[\frac{{\rm Co}^\gamma}{\sqrt{2|B^\gamma|}}\right]^{1/2}\frac{1}{(\chi_\gamma^{(2)})^{1/2}}[1-G^\gamma\chi_\gamma]^{1/2}[1-n\chi_0] . \quad (20)$$

A third experimental probe to determine the B^μ's and K^μ's is the analysis of the softening of the elastic constants. For instance,

$$C^\gamma=C_0^\gamma-(B^\gamma)^2\frac{\chi_\gamma}{1-K^\gamma\chi_\gamma} . \quad (21)$$

This technique has been extensively developed in cubic intermetallics[1] as well as in tetragonal zircons.[4]

From an experimental point of view, the initial step is the knowledge of the CEF, which determines the single-ion susceptibilities. The fit of the first-order magnetic susceptibility along the [001] axis and in the basal plane confirms the CEF parameters and provides us with the bilinear coefficient θ^*. The third-order magnetic susceptibilities, parastrictions, and elastic constants subsequently give the different pairs of B^μ and K^μ coefficients.

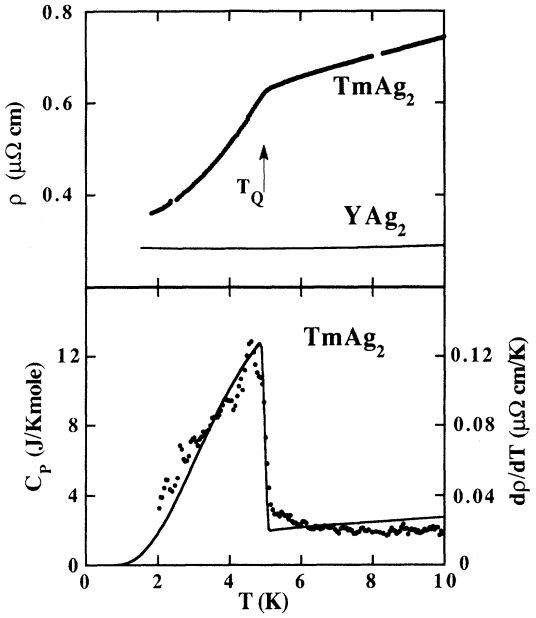

FIG. 1. Low-temperature thermal dependences of the electrical resistivity in $TmAg_2$ and YAg_2 (upper part) and of its derivative (lower part). This latter is normalized by a ratio 93.8 $J/\mu\Omega$ cm to the quadrupolar specific-heat anomaly.

III. THE $TmAg_2$ SYSTEM

All the properties will be described with reference to the $MoSi_2$-type body-centered tetragonal structure [I^4/mmm space group, $a=3.652$, $c=9.140$ Å (Ref. 16)]. The atomic arrangement is generated from a motif of a Tm ion (0,0,0) and a Ag dumbbell (0,0,$\pm z$, with $z=0.327\pm0.003$). Among all the compounds of the series, $TmAg_2$ is the only one which remains paramagnetic.[10] However, it exhibits a specific-heat λ-type anomaly at $T_Q=4.74$ K, which was assumed to be driven by a Jahn-Teller distorsion.[9] a.c. resistivity measurements on monocrystalline and polycrystalline rods and grids clearly reveal the metallic behavior of $TmAg_2$ and YAg_2 (Fig. 1). The progressive loss of resistivity below T_Q is associated with the increasing order parameter. The temperature derivative of the resistivity confirms the second-order character of the transition, which is observed at $T_Q=5.0$ K in our measurements.

Monocrystalline samples were spark cut from a Bridgman ingot: a monocrystalline sphere 3 mm in diameter was used for magnetization and parastriction studies, parallelepipedic samples of typically $3\times3\times3$ mm^3 were used for ultrasonic velocity and magnetostriction measurements. The different axes have been identified by rotating sample x-ray diffraction.

IV. DETERMINATION OF THE CRYSTALLINE ELECTRIC FIELD

Whereas in cubic symmetry the two CEF parameters are usually determined unambiguously by INS, in lower symmetry the increased number of CEF parameters renders the determination of the level scheme more complicated. INS, therefore, has to be interpreted in conjunction with additional experimental probes. In the present case, as for $HoAg_2$,[17] the first-order magnetic susceptibility is used, because it shows clear CEF features and is not influenced by quadrupolar terms. In the disordered phase, the Hamiltonian reduces to

$$\mathcal{H}=\mathcal{H}_{\rm CEF}+\mathcal{H}_B+\mathcal{H}_Z+E_B \ . \tag{22}$$

For Tm ions, the tetragonal symmetry removes the degeneracy of the $J=6$ multiplet into seven singlets and three doublets. The $\mathcal{D}_6$ rotation group reduces to

$$\mathcal{D}_6=2\Gamma_1+\Gamma_2+2\Gamma_3+2\Gamma_4+3\Gamma_5 \ , \tag{23}$$

with the irreducible representations of the $\mathcal{D}_4^h$ point group.[18] The corresponding CEF eigenfunctions are reported in Table II. The off-diagonal V_l^4 terms mix the eigenfunctions within a given set of Γ_i irreducible representations and, therefore, determine first the α, β, γ coefficients in Table II and, second, the intensity of the INS spectrum. J_z, J_+, and J_- transitions can be separated only for large single crystals, which are not available in $TmAg_2$. The lack of these informations for polycrystalline samples may lead to ambiguities in determining the V_l^m's, which have to be resolved by magnetic-susceptibility measurements.

A. Magnetic-susceptibility results

Isothermal magnetization curves were collected along the [001], [100], and [110] directions in fields up to 76 kOe and temperatures ranging from 1.5 to 300 K. The susceptibility values were then deduced in vanishing field (Fig. 2). Within the experimental accuracy, the magnetic susceptibility is isotropic in the basal plane, as expected

TABLE II. The CEF states and eigenfunctions of Tm^{3+} in tetragonal symmetry. In the absence of mixing by V_4^4 and V_6^4 terms, α_1, α_3, α_4, $\alpha_5^{(1)}$, $\beta_5^{(2)}$, and $\gamma_5^{(3)}$ are equal to unity, the other coefficients are null.

$\Gamma_1^{(1)}$	$\alpha_1\dfrac{\lvert4\rangle+\lvert-4\rangle}{\sqrt{2}}+\beta_1\lvert0\rangle$
$\Gamma_1^{(2)}$	$\beta_1\dfrac{\lvert4\rangle+\lvert-4\rangle}{\sqrt{2}}-\alpha_1\lvert0\rangle$
Γ_2	$\dfrac{\lvert4\rangle-\lvert-4\rangle}{\sqrt{2}}$
$\Gamma_3^{(1)}$	$\alpha_3\dfrac{\lvert6\rangle+\lvert-6\rangle}{\sqrt{2}}+\beta_3\dfrac{\lvert2\rangle+\lvert-2\rangle}{\sqrt{2}}$
$\Gamma_3^{(2)}$	$\beta_3\dfrac{\lvert6\rangle+\lvert-6\rangle}{\sqrt{2}}-\alpha_3\dfrac{\lvert2\rangle+\lvert-2\rangle}{\sqrt{2}}$
$\Gamma_4^{(1)}$	$\alpha_4\dfrac{\lvert6\rangle-\lvert-6\rangle}{\sqrt{2}}+\beta_4\dfrac{\lvert2\rangle-\lvert-2\rangle}{\sqrt{2}}$
$\Gamma_4^{(2)}$	$\beta_4\dfrac{\lvert6\rangle-\lvert-6\rangle}{\sqrt{2}}-\alpha_4\dfrac{\lvert2\rangle-\lvert-2\rangle}{\sqrt{2}}$
$\Gamma_5^{(1)}$	$\alpha_5^{(1)}\lvert\pm5\rangle+\beta_5^{(1)}\lvert\pm3\rangle+\gamma_5^{(1)}\lvert\pm1\rangle$
$\Gamma_5^{(2)}$	$\alpha_5^{(2)}\lvert\pm5\rangle+\beta_5^{(2)}\lvert\pm3\rangle+\gamma_5^{(2)}\lvert\pm1\rangle$
$\Gamma_5^{(3)}$	$\alpha_5^{(3)}\lvert\pm5\rangle+\beta_5^{(3)}\lvert\pm3\rangle+\gamma_5^{(3)}\lvert\pm1\rangle$

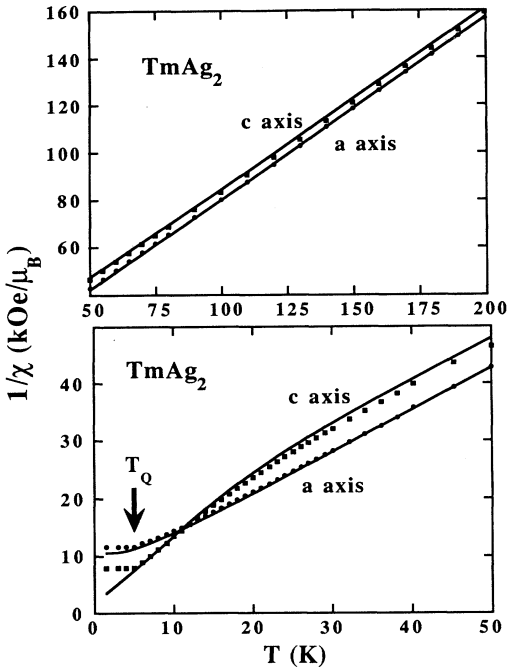

FIG. 2. The temperature dependence of the reciprocal first-order magnetic susceptibility along the c axis and in the basal plane. Full lines are calculated within the tetragonal symmetry. T_Q is the γ-quadrupolar transition.

for the tetragonal symmetry.

At high temperature, the reciprocal susceptibility is least in the basal plane. However, the anisotropy is relatively weak: $\Delta\chi^{-1}=\chi^{-1}_{[001]}-\chi^{-1}_{[100]}\approx 3$ kOe/μ_B at 300 K. Both temperature variations are parallel above 100 K. Their slope leads to a Curie constant of 1.285 kOe K/μ_B (7.18 K/cm^3), a value close to the free-ion value (7.16). As in $HoAg_2$, this behavior indicates that (i) the contribution of conduction electrons to the magnetic susceptibility is weak, and (ii) only the second-order CEF term is sizable at high temperature: indicative values of V_2^0 and n may be deduced from expressions in Ref. 19:

$$\chi^{-1}_{[001]}-\chi^{-1}_{[110]}=\frac{3}{2}\frac{(2J-1)(2J+3)}{5C}\alpha_J V_2^0 ,$$
$$\chi^{-1}_{[001]}(T)+2\chi^{-1}_{[110]}(T)=3\frac{T-\theta^*}{C} . \quad (24)$$

V_2^0 and θ^* are about 7 and -2 K, respectively.

With decreasing temperature, the anisotropy of the susceptibility decreases and changes sign around 11.5 K. At lower temperature, the direction of easy magnetization is the c axis. Qualitatively, this results from the increasing role played by higher-order CEF terms V_4^m and V_6^m, which overcome the V_2^0 term at low temperature.

B. Inelastic neutron spectroscopy results

The INS experiments were performed at the Institute Laue-Langevin high flux reactor on the *IN*4 time-of-flight spectrometer, with incident neutron energy $E_0=17$ meV. A total of 49 detectors were positioned at scattering angles ranging from 11° to 101°. Their relative efficiencies were calibrated by means of a Vanadium scatterer. The elastic resolution was about 0.7 meV. The samples were polycrystalline plates of optimum thickness for $E_0=17$ meV, typically 1.5 mm. Background scattering, measured without a sample, was subtracted after correction for the sample transmission to give the normalized cross section. Additional data were collected with the low-incident energy spectrometer *IN*6 ($E_0=3.16$ meV) in order to detect the possible existence of low-lying levels close to the ground state.

Among the $E_0=17$-meV spectra, we first consider the 8-K spectrum, which results from excitations from the ground state and very low-lying levels. Immediately above T_Q, i.e., in the tetragonal phase, six transitions are observed at 1.25, 3.8, 5.1, 7.7, 9.0, and 10.1 meV (Fig. 3). Spectra at higher temperatures are marked by the growth of deexcitation processes. Due to the presence of numerous transitions between excited levels, the inelastic profiles are smooth. These high-temperature spectra are analyzed only in order to check consistency with the level scheme deduced at low temperature. With $E_0=3.16$ meV, the CEF origin of the low-temperature excitations

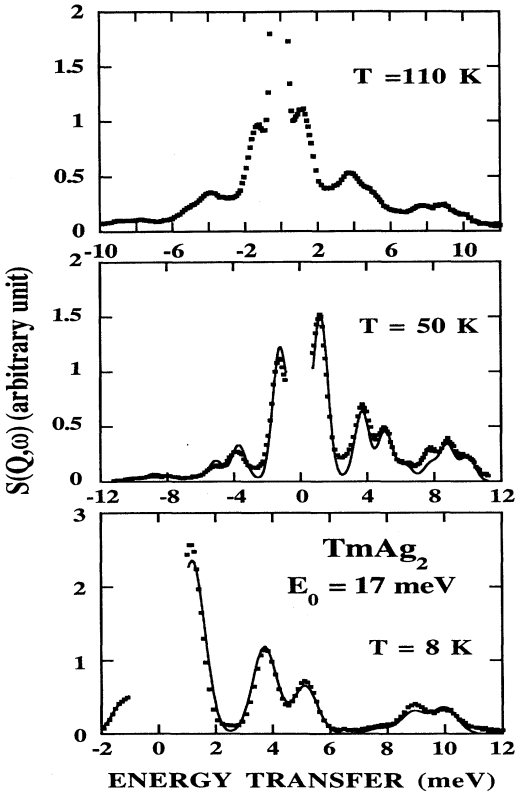

FIG. 3. Inelastic neutron-scattering spectra with incident energy $E_0=17$ meV collected at different temperatures in $TmAg_2$, with the *IN*4 spectrometer (squares). For the fit (full lines) at 8 and 50 K, the elastic and quasielastic peaks have been removed. The same V_l^m parameters are used here as for Fig. 2: $V_2^0=9$ K, $V_4^0=2$ K, $V_4^4=-395$ K, $V_6^0=-16$ K, and $V_6^4=230$ K.

is well confirmed by their temperature dependences (Fig. 4). The analysis of the spectrum at 1.6 K, below T_Q, will be discussed in Sec. VI A.

C. The crystalline electric field

The description of both types of experimental data was achieved with the same self-consistent diagonalization of Eq. (22) by a least-squares procedure as for $HoAg_2$. In a first step, V_2^0 and θ^* were kept at the value estimated from the high-temperature susceptibility data (7 and -2 K, respectively); V_4^m and V_6^m were the four variable parameters. In spite of the peculiarities of the susceptibility (the change of easy magnetization direction at 11.5 K) and of the large number of CEF excitations observed at 8 K, the search leads to a great number of V_l^m sets for each experiment, without a clear common solution. This is closely reminiscent of the conclusions for the same analysis applied to $HoAg_2$.

In the next step, each partial solution is tested against the other experimental results. The search for the best compromise is then realized by successive cross checks between fits of magnetic data and of the 8-K spectrum. In all the fits (Figs. 2 and 3), V_6^0 and V_6^4 rapidly converge to -16 ± 1.5 and 230 ± 10 K, respectively. The V_4^0 parameter is weak and equals 2 ± 3 K. $V_4^4=-395\pm20$ K. Treating V_2^0 as a free parameter does not drastically change its weak value: $V_2^0=9\pm3$ K. Bilinear interactions are characterized by $\theta^*=-2.5\pm0.2$ K. As for $HoAg_2$, again, varying the different parameters within their uncertainty ranges does not alter noticeably the level scheme and eigenfunctions.

The CEF level spacing and eigenfunctions are reported in Table III. The large V_l^4 coefficients drive the large mixing of the eigenfunctions. Only the levels lower than 12 meV can be observed within the $E_0=17$-meV incident energy. The excitations to the four highest energy levels are calculated to be weak. They were observed at 8 K using an $E_0=68$-meV incident energy around 14 and 16 meV in agreement with this level spacing, however superimposed with phonon contributions. Our trust in this set of V_l^m is reinforced by the comparison with the set obtained in $HoAg_2$ ($V_2^0=47\pm10$ K, $V_4^0=6\pm3$ K, $V_4^4=-390\pm20$ K, $V_6^0=-15$ K, and $V_6^4=+195\pm5$ K). This nice coherency is the signature of constant contributions to the CEF throughout the series. Preliminary analyses of results obtained in $ErAg_2$ also confirm this conclusion. CEF properties appear to be ruled by large mixing parameters V_4^4 and V_6^4. The relative weakness of diagonal terms, especially V_2^0, explains the frequent existence of changes of the easy magnetization direction between the c axis and the basal plane (one in $TmAg_2$, two in $HoAg_2$).

$TmAg_2$ and $HoAg_2$ demonstrate the necessity of complementary experimental probes in addition to neutron spectroscopy. Magnetic susceptibility is very relevant to

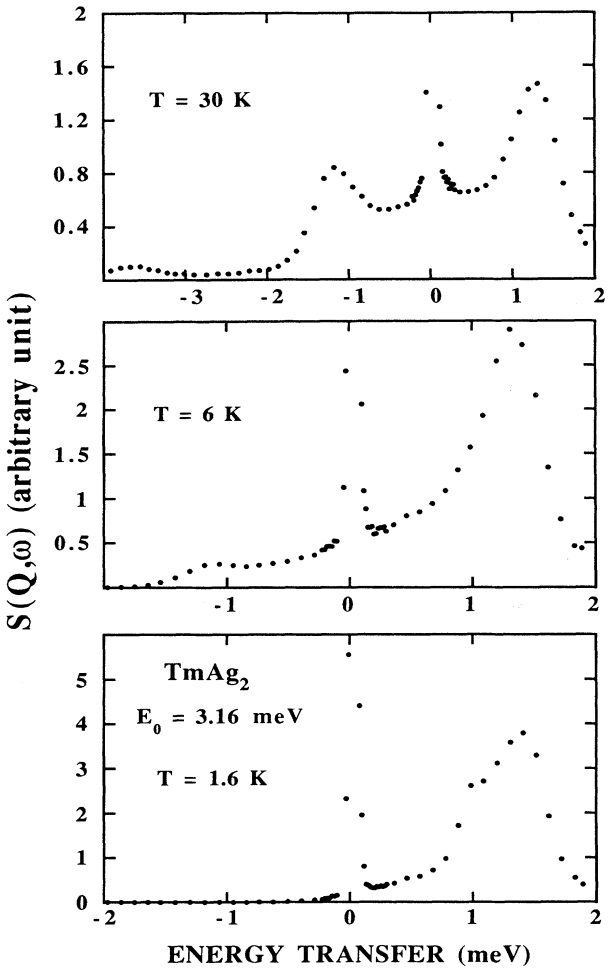

FIG. 4. *IN*6 spectra collected in $TmAg_2$ with incident energy $E_0=3.16$ meV at the temperature indicated.

TABLE III. (Upper) CEF energy levels (in K) and eigenfunctions calculated for the parameters $V_2^0=9$, $V_4^0=2$, $V_4^4=-395$, $V_6^0=-16$, and $V_6^4=+230$ K. The exponent of each Γ_i is labeled, in agreement with Table II, according to the maximum component of the eigenfunctions. (Lower) Nature of the excitations observed at 8 K with $E_0=17$ meV as incident energy.

190.4	$\Gamma_3^{(2)}$	$\alpha_3=0.719$ $\beta_3=-0.694$
176.4	$\Gamma_4^{(1)}$	$\alpha_4=0.772$ $\beta_4=0.635$
160.3	$\Gamma_1^{(1)}$	$\alpha_1=0.784$ $\beta_1=0.621$
158.2	$\Gamma_5^{(3)}$	$\alpha_5^{(3)}=0.506$ $\beta_5^{(3)}=-0.542$ $\gamma_5^{(3)}=0.671$
116.2	$\Gamma_5^{(2)}$	$\alpha_5^{(2)}=0.450$ $\beta_5^{(2)}=-0.829$ $\gamma_5^{(2)}=0.330$
103.8	Γ_2	
59.5	$\Gamma_3^{(1)}$	$\alpha_3=0.719$ $\beta_3=-0.694$
43.1	$\Gamma_4^{(2)}$	$\alpha_4=0.772$ $\beta_4=0.635$
14.0	$\Gamma_1^{(2)}$	$\alpha_1=0.784$ $\beta_1=0.621$
0	$\Gamma_5^{(1)}$	$\alpha_5^{(1)}=0.735$ $\beta_5^{(1)}=0.135$ $\gamma_5^{(1)}=-0.664$

Δ (K)	
14.5	$\langle\Gamma_5^{(1)}\|J_x\|\Gamma_1^{(2)}\rangle$
44	$\langle\Gamma_5^{(1)}\|J_x\|\Gamma_4^{(2)}\rangle$
59	$\langle\Gamma_5^{(1)}\|J_z\|\Gamma_3^{(1)}\rangle$
90	$\langle\Gamma_1^{(2)}\|J_z\|\Gamma_2\rangle$
104	$\langle\Gamma_5^{(1)}\|J_x\|\Gamma_2\rangle;\langle\Gamma_1^{(2)}\|J_x\|\Gamma_5^{(2)}\rangle$
117	$\langle\Gamma_5^{(1)}\|J_z\|\Gamma_5^{(2)}\rangle$

this procedure because it does not introduce additional parameters, except for the bilinear exchange coefficient θ^*. Conclusions pointed out during the study of $HoAg_2$ are confirmed. V_2^0 is clearly smaller than observed in intermetallics within hexagonal or tetragonal symmetry (from 100 to 500 K, according to the series). Studying the surroundings of a R ion in RAg_2 reveals that it is not too far from cubic symmetry. A crude point charge estimate considering the c/a ratio, the z dimension of the Ag dumbbell, and Ag^+ and R^{3+} ionic states describes the V_2^0 value perfectly, although somewhat fortuitously. Indeed, it is well accepted that CEF parameters result from a balance between the contributions from point charges and the conduction band.[20] However, since the symmetry of the ligands determines at least partly the symmetry of the band close to the $4f$ site, both types of contribution to V_2^0 may be expected to be weak.

The other parameters behave more normally. For instance, in the cubic CsCl-type series, involving RAg, V_6^0 and V_6^4 are quasi-independent of the compound considered and close to -15 and $+315$ K, respectively.[21] The values observed in $HoAg_2$ and $TmAg_2$ are not too far from these, although the ratio $V_6^4/V_6^0=-21$ for cubic symmetry changes to around -14. Within the CsCl-type series, averaged values are -40 K for V_4^0, which gives -200 for V_4^4; in RAg_2, the absolute value of V_4^0 is small and the ratio V_4^4/V_4^0 differs considerably from the value required for cubic symmetry ($V_4^4/V_4^0=5$). In conclusion, as in any metallic series, the CEF parameter can be explained only if the electronic contributions calculated from an accurate knowledge of the conduction band is considered character by character (s,p,d,f), as was done for CsCl-type compounds.[20]

Note that INS and first-order magnetic-susceptibility measurements lead to the conclusion that V_4^4 and V_6^4 have opposite sign. According to their respective signs, x and y axes are related to either the $\langle 100\rangle$ axes or the $\langle 110\rangle$ axes of the body-centered cell; this results from the properties of the $\mathcal{D}_4^h$ rotation group. The correct set of V_4^m related to the $\langle 100\rangle$ axes can be determined only by studying anisotropic properties within the basal plane, as is done in Sec. V. The description of our data will only be possible with the above set ($V_4^4=-390$ K and $V_6^4=+230$ K) due to temperature dependences that are clearly different for the single-ion susceptibilities.

In $TmAg_2$, the ground state is then a doublet $\Gamma_5^{(1)}$ built essentially from the $|\pm5\rangle$ and $|\pm1\rangle$ components. The magnetic behavior of this doublet ($\langle J_z\rangle=\pm3.09$) would lead to an antiferromagnetic ordering, with the c axis as the easy magnetization direction, if the quadrupolar ordering did not occur at a higher temperature. The $\langle\Gamma_5^{(1)}|O_2^0|\Gamma_5^{(1)}\rangle=0.37$ matrix element is small, in accord with the weak anisotropy between axes at low temperature (Fig. 2). Due to this small value, the quadrupolar interaction energy within the α symmetry, $G^\alpha\langle O_2^0\rangle^2$, is reduced, and a quadrupolar transition at T_Q, keeping the tetragonal symmetry, would require huge G^α values, which is very unlikely. On the contrary, the orbital degeneracy of the $\Gamma_5^{(1)}$ doublet may be removed by γ or δ orthorhombic symmetry-lowering modes. Indeed, the matrix elements $\langle\Gamma_{5,1}^{(1)}|O_2^2|\Gamma_{5,2}^{(1)}\rangle=15.21$ and $\langle\Gamma_{5,1}^{(1)}|P_{xy}|\Gamma_{5,2}^{(1)}\rangle=4.20$ are large. According to the strength of the total quadrupolar coefficients G_γ, G_δ, a quadrupolar ordering of orthorhombic symmetry can occur at T_Q, requiring, however, a weaker coefficient for the γ symmetry.

The following set of CEF parameters, $V_2^0=9$ K, $V_4^0=2$ K, $V_4^4=-395$ K, $V_6^0=-16$ K, and $V_6^4=230$ K, as well as the bilinear exchange temperature, $\theta^*=-2.5$ K, will be kept *fixed* in all following sections.

V. MAGNETIC AND MAGNETOELASTIC PROPERTIES IN THE TETRAGONAL PHASE

A. Third-order magnetic susceptibility

For the $4/mmm$ symmetry class, the description of the magnetization requires polar tensors H_m of even rank.[22] In the notations of Birss, the fourth-rank H_4 tensor includes five elements $xxxx$, $zzzz$, $xxyy$, $xxzz$, and $zzxx$, which are associated with the γ-, α-, δ-, and ε-symmetry-lowering modes, respectively. As stated in Sec. II, the ε case is not considered here. For a high-symmetry field direction, the expressions are very simple and reduce to Eqs. (16).

The set of isothermal magnetization curves, which previously gave us the anisotropic first-order susceptibility, is used again here (Fig. 5). The initial slope of M/H as a function of H^2 is obviously positive along the **a** axis, whereas it remains negative along the **c** and **b** directions, as classically expected. The $\chi_M^{(3)}$ temperature dependences are reported in Figs. 6–8. Along the **c** axis, data are described only by bilinear interactions with $\theta^*=-2.5$ K. Introducing a nonzero G^α contribution produces a worse fit to the data, in particular at high temperatures (Fig. 6). This results from the $\langle O_2^0\rangle$ values, which are very different within the ground state (0.37) and the first excited singlet (-23.5). This constitutes the first evidence of weak α-symmetry quadrupolar interactions. The same conclusion is also valid along the **b** axis (Fig. 7). Varying θ^* within its uncertainty range induces changes

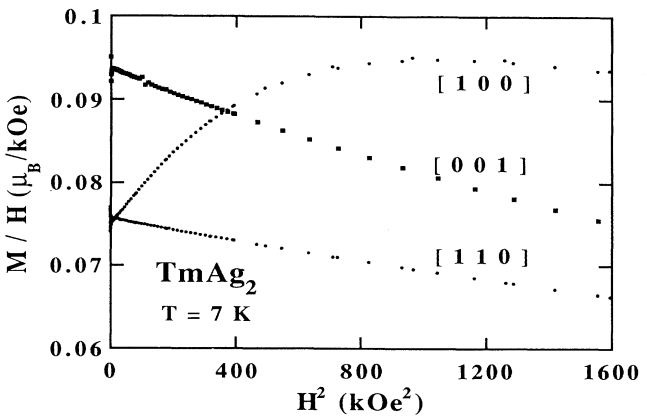

FIG. 5. Plots of $(M/H)/(H^2)$ along the main crystallographic directions of the tetragonal phase at 7 K in $TmAg_2$.

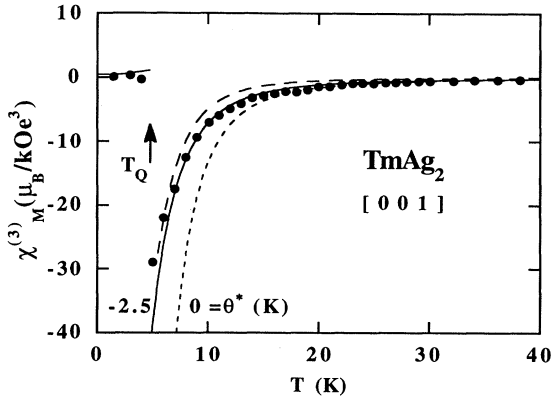

FIG. 6. The temperature variation of the third-order magnetic susceptibility along the **c** axis in the tetragonal and orthorhombic phases. Curves are calculated without any interaction (dotted line) or with bilinear temperatures ($\theta^*=-2.5$ K) (full line: without α-quadrupolar interactions; hatched line: in the presence of α interactions characterized by $G^\alpha=15$ mK).

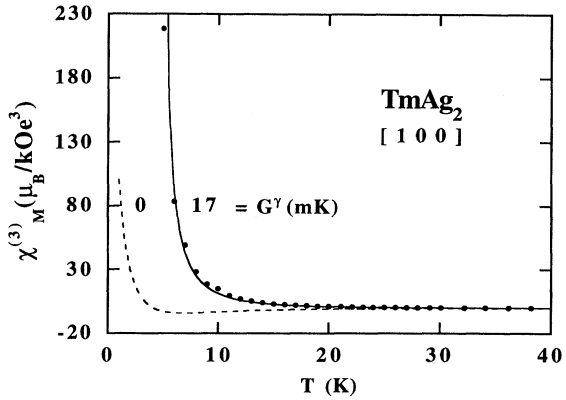

FIG. 8. The temperature variation of the third-order magnetic susceptibility along the **a** axis of the body-centered tetragonal cell. Curves are calculated with $\theta^*=-2.5$ K and γ-quadrupolar contributions either null (hatched curve) or defined by $G^\gamma=17$ mK.

larger than varying G^α or G^δ. Here again, G^α is close to zero ($G^\alpha=0\ \pm3$ mK). G^δ appears small ($G^\delta=0\pm10$ mK).

Along the **a** axis, $\chi_M^{(3)}$ is positive up to 40 K (Fig. 8). Obviously, positive G^α values are needed for a good description, which is achieved with $G^\gamma=17\pm1$ mK. Here again, the fit does not exhibit a great dependence on G^α; in addition, the large values necessary would induce a temperature variation clearly different from the experimental one.

B. Parastriction

Data have been obtained with a capacitance dilatometer[23] under magnetic fields up to 5 kOe with a sensitivity of 1 Å and an accuracy of 1% for temperatures from 6 to 300 K. The size of the monocrystalline sphere, about 3 mm in diameter, limits the relative change of length to 4.10^{-8}. At every temperature the quadratic field dependence of the measured strength has been checked. In the case of small strain, sensitivity is limited by the field available in this apparatus. Complementary data have been collected with strain gauges (sensitivity around 2.10^{-7}) in fields up to 50 kOe and in temperatures from 1.6 to 250 K. As explained in Sec. II, linearized temperature variations are analyzed with equations similar to Eq. (20).

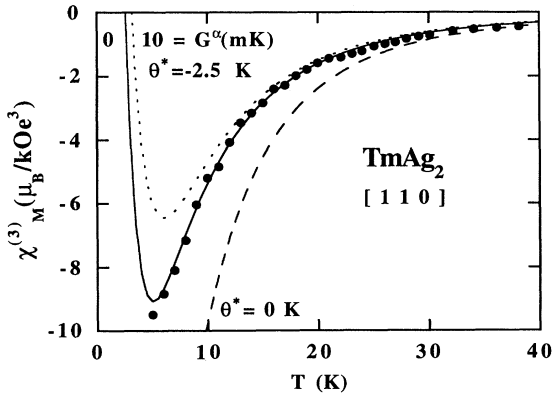

FIG. 7. The temperature variation of the third-order magnetic susceptibility along the **b** axis of the body-centered tetragonal cell. Curves are calculated with $\theta^*=0$ (hatched line) and with $\theta^*=-2.5$ K (full line: without any quadrupolar contribution; dotted line: with a $G^\alpha=10$-mK quadrupolar term).

The γ-symmetry-lowering mode has been studied with a magnetic field applied along the [100] axis, the change of length ($\lambda_\parallel,\lambda_\perp$) being measured parallel and perpendicular to it:

$$\lambda_{[100]}^{[100]}=\lambda_\parallel=\frac{\varepsilon^{\alpha1}}{\sqrt{3}}-\frac{1}{\sqrt{6}}\varepsilon^{\alpha2}+\frac{1}{\sqrt{2}}\varepsilon^{\gamma}\ ,$$
$$\lambda_{[100]}^{[010]}=\lambda_\perp=\frac{\varepsilon^{\alpha1}}{\sqrt{3}}-\frac{1}{\sqrt{6}}\varepsilon^{\alpha2}-\frac{1}{\sqrt{2}}\varepsilon^{\gamma}\ . \qquad (25)$$

The fact that $\lambda_\parallel$ and $\lambda_\perp$ are opposite within the experimental accuracy confirms that ε^α is negligible in comparison to ε^γ. The difference $\lambda_\parallel-\lambda_\perp=\sqrt{2}\varepsilon^\gamma$ is negative, thus B^γ also is. The linearized temperature variation is compared to Eq. (20) in Fig. 9: the slope gives B^γ, the vertical shift from the behavior with only θ^* gives G^γ. A good agreement is observed with the G^γ value obtained in Sec. V A: $G^\gamma=18\pm2$ mK. The background constant $C\zeta=14.2\ 10^4$ K/at leads to $B^\gamma=-31\pm2$ K/at. Note that the calculated variation leads to a spontaneous strain at 5 K, i.e., at the experimental value for T_Q (see Sec. VI).

The same procedure was followed for the δ symmetry and changes of length along [110] and [1$\bar{1}$0], with the field along the [110] axis. These magnetoexpansions are given by equations similar to Eq. (25). Here again, $\lambda_\parallel$ and $\lambda_\perp$ are opposite, but about 100 times smaller than for the γ symmetry. The opposite sign indicates the α contributions are negligible. The small values may be the signature of a weak δ-symmetry magnetoelastic coupling. However, it is difficult to analyze these data as due only

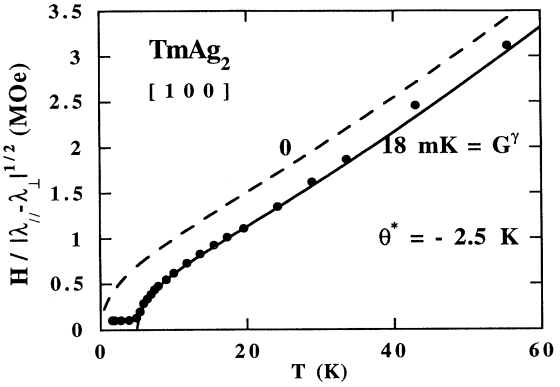

FIG. 9. The temperature variation of the parastriction within the γ symmetry. Curves are calculated with $\theta^* = -2.5$ K, with or without γ-quadrupolar interactions. Below $T_Q = 5$ K, data correspond to "destraining" effects associated with the partition of the sample into strain domains (see Fig. 16).

to the δ coupling. Indeed a misorientation of 3° between the [110] axis and the field direction could, by itself, drive such $\lambda_{\parallel}^{[110]} - \lambda_{\perp}^{[110]}$ values. The temperature dependence of the data indicate the two contributions are antagonistic, i.e., B^{δ} is weakly positive. The γ-symmetry-lowering mode is here confirmed to overwhelm the α- and δ-symmetry ones.

C. Ultrasonic velocity

Elastic constants were determined from velocity measurements of ultrasonic longitudinal and transverse waves propagating along the [001], [100], and [110] directions. The pulse-echo overlap method was used. Data was taken by decreasing the temperature from 300 K. Only the C_{11}-C_{12} mode is discussed here. It exhibits a very pronounced softening which, at 7 K, reaches $\sim 50\%$ of the low-temperature value expected from YAg_2 (Fig. 10). Echoes are lost below 7 K due to the damping of the elastic wave. This softening is described by Eq. (21). The C_0^{γ} lattice behavior is deduced from the YAg_2 one: the temperature dependence exhibits the same slope, only the 300-K absolute value is adjusted. The fit leads to the (B^{γ}, K^{γ}) pairs varying from (30 K, 11 mK) to (37 K, 3 mK): this range of solutions includes the values previously observed in Secs. V A and V B. The full study of the elastic constants will be presented in a forthcoming paper.[24]

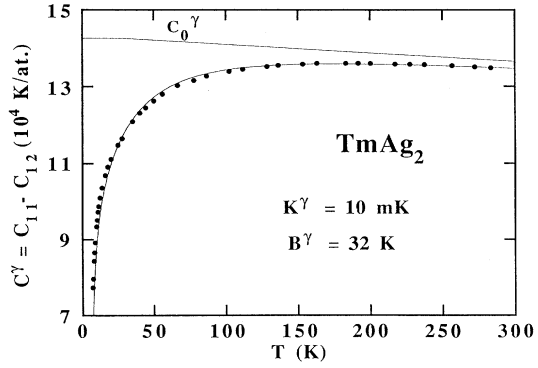

FIG. 10. The temperature dependence of the $C^{\gamma} = C_{11} - C_{12}$ ultrasonic mode. C_0^{γ} is the background elastic constant deduced from measurements in YAg_2. The full curve is a fit using the parameters indicated.

TABLE IV. Quadrupolar parameters determined in $TmAg_2$ for the orthorhombic γ-symmetry-lowering mode.

	B^{γ} (K)	K^{γ} (mK)	G^{γ} (mK)
$\chi_M^{(3)}$			17
Parastriction	−31		18
$C^{\gamma} = C_{11} - C_{12}$	±31	+10	17
T_Q			18

D. Conclusion

To conclude this section, the CEF parameters are well confirmed by the quality of the fits. The three experimental probes specifically devoted to quadrupolar interactions lead to a great coherency between independent determinations (Table IV). Quadrupolar interactions are obviously present in $TmAg_2$, associated with the γ-symmetry-lowering mode. The other α and δ normal modes are strongly unfavored and, for instance, the determination of ε^{α} and ε^{δ} is made difficult by the γ contribution introduced through any misorientation. This task is complicated by the weakness of both the magnetoelastic coefficients and the susceptibilities. We plan to follow the B^{α} and B^{δ} coefficients in a specific study.[24]

The B^{γ} value agrees with values usually obtained in rare-earth intermetallics. According to its one-ion origin, renormalization by the α_J Stevens coefficient leads to $B^{\gamma}/\alpha_J = -3100$ K/at, as for instance in CsCl-type cubic intermetallics and in RXO_4 (X=V,As,P) insulators.[1] The magnetoelastic contribution to G^{γ}, $(B^{\gamma})^2/C_0^{\gamma} = 7$ mK, is slightly smaller than the pair interactions ($K^{\gamma} = 10$ mK) between the $4f$ sites. The $TmAg_2$ case is reminiscent of the situation for TmZn and TmCd cubic intermetallics, where the dominating pair interactions ($K^{\gamma}/G^{\gamma} = \frac{4}{5}$ and $\frac{11}{12}$, respectively) are the driving mechanism for the quadrupolar ordering, and where the lattice distortion may be mainly considered to be a consequence of the quadrupolar ordering through the magnetoelastic coupling. The competition between both interactions is, however, better balanced in $TmAg_2$ ($K^{\gamma}/G^{\gamma} = \frac{10}{18}$). Note that the case of tetragonal insulators RXO_4 is the opposite, for which the magnetoelastic coupling is responsible for the structural transition ($K^{\gamma}/G^{\gamma} \approx -\frac{1}{2}$).

VI. LOW-TEMPERATURE PROPERTIES

A. The γ-quadrupolar transition

For a second-order transition, it is well known that the susceptibility associated with the order parameter, here χ_{γ} and $\langle O_2^2 \rangle$, respectively, diverges at the ordering transition. Figure 11 gives the relationship between G^{γ} and

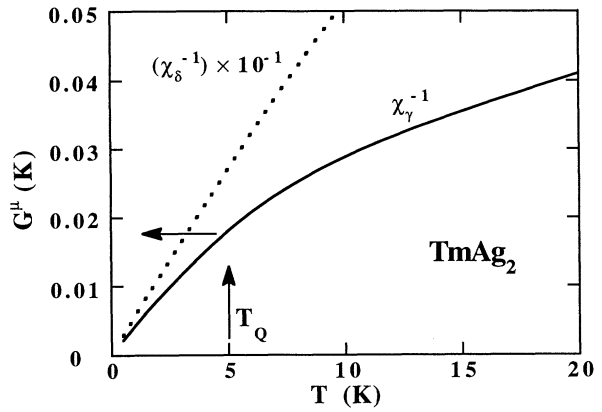

FIG. 11. Relationships between the total quadrupolar coefficients and the temperature for the γ and δ orthorhombic-symmetry-lowering modes. $T_Q=5$ K is driven by $G^\gamma=18$ mK. Since χ_δ is divided by a factor of 10, G^δ has to be multiplied by the same 10 factor.

T_Q from the temperature variation of χ_γ^{-1}. A perfect agreement is observed between the experimental values $G^\gamma=18$ mK and $T_Q=5$ K. The second-order character of the transition is confirmed by the temperature dependence of $\langle O_2^2 \rangle$ calculated by the diagonalization of Eq. (1). It is drawn in Fig. 12 with the $\langle O_2^0 \rangle$ thermal variation. The same calculation also gives the thermal behavior of the specific heat, which is compared, in the absence of data, to the resistivity derivative (Fig. 1). Within the experimental accuracy, both curves represent the same variation of the quadrupolar energy.

Also drawn in Fig. 11, the thermal variation of χ_δ^{-1} shows how unfavored the δ-symmetry-lowering mode is. A δ-quadrupolar ordering at 5 K needs a $G^\delta=250$-mK value, i.e., 14 times larger than for the γ case.

The behavior of $\langle O_2^0 \rangle$, then, of the tetragonal CEF level scheme, has also been studied as a function of only G^α (Fig. 12). For G^α weaker than 37.5 mK, only the $\langle O_2^0 \rangle$ amplitude is changed and a "breathing" of the CEF level spacing is induced by the apparent second-order CEF term $(V_2^0+G^\alpha\langle O_2^0 \rangle)$. For G^α larger than 40 mK, the ground-state doublet $\Gamma_5^{(1)}$ is replaced by the $\Gamma_1^{(2)}$ singlet, which is characterized by a large negative $\langle O_2^0 \rangle$ value. The eigenfunctions are also significantly modified. For G^α larger than 54 mK, a completely different level scheme results. As in the previous experiments, these calculations confirm that quadrupolar α interactions are not involved in the quadrupolar transition for $TmAg_2$.

The temperature variation of the energy of the low-lying levels is drawn in Fig. 13. Note that the splitting of the tetragonal symmetry $\Gamma_5^{(1)}$ doublet is not strictly symmetrical in the orthorhombic phase due to the off-diagonal matrix elements $\langle \Gamma_{51}^{(1)}|J_z|\Gamma_{52}^{(1)}\rangle=3.1$, $\langle \Gamma_{51}^{(1)}|J_x|\Gamma_1^{(2)}\rangle=4.5$, and $|\langle \Gamma_{52}^{(1)}|J_y|\Gamma_1^{(2)}\rangle|=2.7$. They lead to two excitations from $\Gamma_{51}^{(1)}$, the ground-state singlet in the orthorhombic phase, which are observed by INS with incident energy $E_0=3.16$ meV (Fig. 4). The $\langle \Gamma_{52}^{(1)}|J_y|\Gamma_1^{(2)}\rangle$ excitation is weak at 1.6 K due to thermal effects, but can be distinguished at the expected transfer. Calculations also explain the INS spectra at 3 and 4 K (Fig. 13). These preliminary results motivate a forthcoming study of excitations in a large single crystal.

B. Magnetization properties

1. [001] axis

For a magnetic field along the c axis, the magnetic response exhibits very different features depending on the paramagnetic phase considered (Fig. 14). Instead of a Brillouin-type variation as at 6 K, low-temperature curves are characterized by two different linear regimes. Calculations with the previous V_l^m and θ^* and $G^\gamma=18$ mK perfectly describe the initial variation and the high-

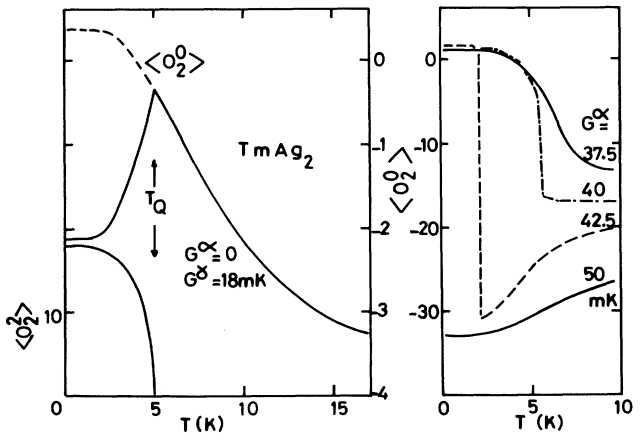

FIG. 12. The temperature variation of the two $\langle O_2^0 \rangle$ and $\langle O_2^2 \rangle$ quadrupolar components in the tetragonal and orthorhombic phases (left part). The temperature dependence of $\langle O_2^0 \rangle$ in the presence of only α-quadrupolar contributions, as indicated by the G^α values (right part).

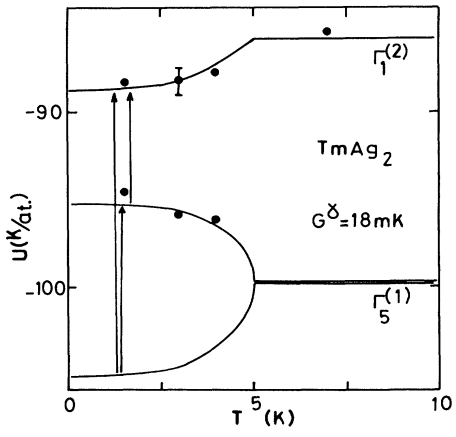

FIG. 13. The temperature dependence of the low-lying CEF levels in the tetragonal and orthorhombic phases of $TmAg_2$. The arrows correspond to CEF excitations as observed in Fig. 4, and dots to the corresponding energy transfers.

field regime. In the intermediary range (from about 5 up to 35 kOe), a slight overestimation of the calculated magnetization is observed, which may be explained by the existence of magnetostrictive stresses. The change in slope of the magnetization corresponds to the field breaking of the orthorhombic phase, as indicated by the calculated field variation of $\langle O_2^2 \rangle$. The corresponding critical field is given as a function of temperature in Fig. 14.

As stated above, the initial susceptibility is well described in the orthorhombic phase because it is not influenced by the partition of the sample into orthorhombic strain domains, which only determine the properties within the basal plane (Fig. 15). The thermal variation of the third-order magnetic susceptibility is also calculated to be in close agreement with the data in the paramagnetic orthorhombic phase (see Fig. 6).

2. *[100] axis*

At high temperature, magnetization curves are well described by the calculations (Fig. 16). Only a small excess of the magnetic moment (less than $0.15\mu_B$) is observed, which again can originate from magnetoelastic stress. At low temperature, this shift occurs in zero field. The field necessary to cancel the unfavored orthorhombic domain may be estimated to be 10 kOe, calculated and experimental curves being parallel above this value (Fig. 16). The inflexion point of the magnetization curves in the tetragonal phase is calculated as a crossover between the tetragonal phase, orthorhombically strained, and the true γ-quadrupolar phase (Fig. 17).

The χ_{a0} and χ_{b0} susceptibilities along the a_0 and b_0 axes of the orthorhombic cell are calculated to be very different, the a_0 axis being the easy magnetization direction. For instance, at 1.6 K,

$$\chi_{a0}=0.2325\mu_B/\text{kOe} ,$$

$$\chi_{b0}=0.0128\mu_B/\text{kOe} .$$

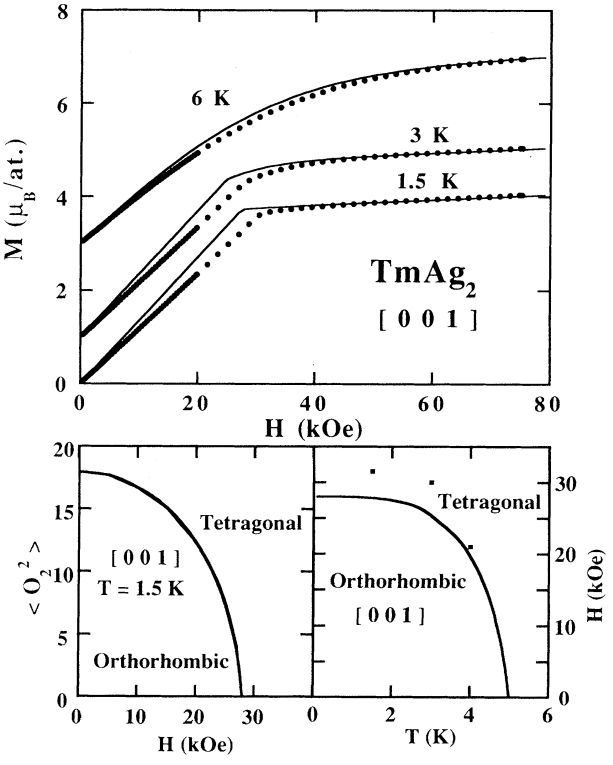

FIG. 14. Experimental and calculated magnetization curves for a magnetic field along the c axis (upper part). The 6- and 3-K curves are shifted upwards by 3 and $1\mu_B$, respectively. The change in slope at low temperature corresponds to the field breaking of the orthorhombic phase as indicated by the calculated vanishing of $\langle O_2^2 \rangle$ at 1.5 K (lower part). Also drawn is the (H,T) orthorhombic-tetragonal phase diagram; black squares are experimental.

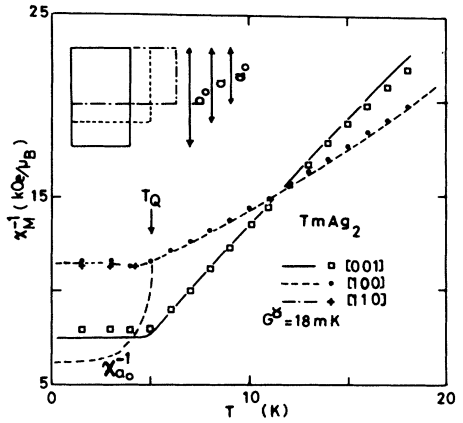

FIG. 15. The temperature variation of the first-order magnetic susceptibility at low temperature along the three main directions of the tetragonal cell. Lines are calculated with $G^\gamma=18$ mK; $\chi_{a_0}^{-1}$ is the reciprocal susceptibility along the [100] binary axis of the orthorhombic cell.

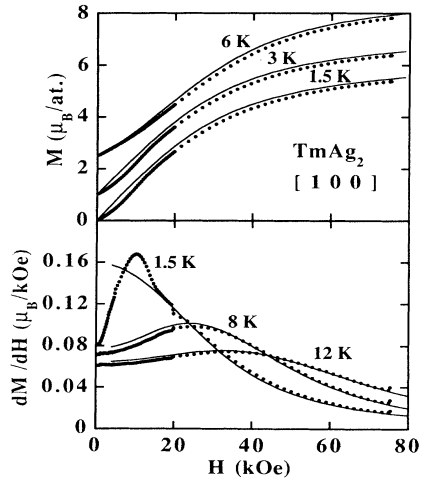

FIG. 16. Experimental and calculated magnetization curves along the [100] direction of the tetragonal and orthorhombic phases. The 6- and 3-K curves are shifted upwards by 2.5 and $1\mu_B$, respectively. The different behaviors in low field are due to the move of strain domains in the orthorhombic phase.

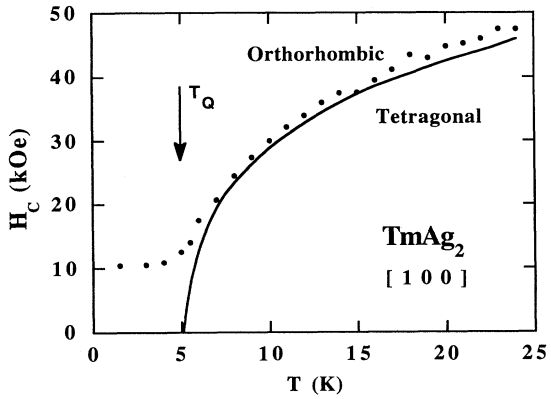

FIG. 17. Temperature dependence of the critical field corresponding to the inflection point of the [100] magnetization curves (dots: data; the full curve is calculated with $G^{\gamma}=18$ mK). Dots below T_Q correspond to the move of strain domains (see Figs. 16 and 9).

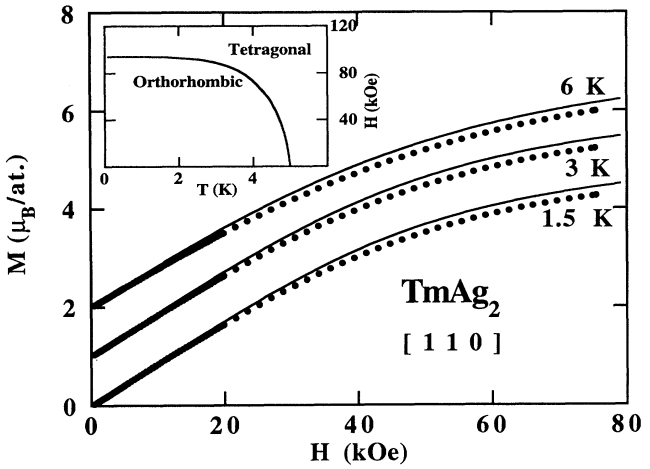

FIG. 18. Magnetization curves measured and calculated along the [110] axis of the tetragonal cell. The 6- and 3-K curves are shifted upwards by 2 and $1\mu_B$, respectively. The inset gives the orthorhombic-tetragonal phase diagram calculated for a [110] field direction.

The susceptibility measured along the [100] tetragonal axis, $\chi^{[100]}$, is then determined by the strain domain partition $\chi^{[100]}=\alpha\chi_{a0}+(1-\alpha)\chi_{b0}$, with α smaller than unit. Its values (for instance, $0.086\mu_B$/kOe at 1.6 K) indicates an exact equipartition (Fig. 15).

3. *[110] axis*

Figure 18 gives characteristic magnetization curves for the magnetic field pointing along a [110] axis of the tetragonal cell. The magnetization processes are well described by the calculations; below T_Q, they do not exhibit clear features, which could indicate the field-induced breaking of the orthorhombic symmetry. This crossover to the δ-strained tetragonal structure has been calculated through the vanishing of the $\langle O_2^2 \rangle$ quadrupolar moment: the inset of Fig. 18 indicates that large field values are needed.

For a field along a $\langle 110 \rangle$ tetragonal axis, i.e., at 45° from the a_0 axis in both orthorhombic domains, the susceptibility is not determined by the partition into domains, and reads as the mean of χ_{a0} and χ_{b0}. Calculated values are in close agreement with experiment (Fig. 15). Note that the identity between $\chi^{[100]}$ and $\chi^{[110]}$ is the signature of an equipartition for strain domains.

VII. CONCLUSION

This study of the magnetic and magnetoelastic properties in $TmAg_2$ reveals the existence of a quadrupolar ordering in a rare-earth intermetallic with the tetragonal symmetry. The high quality of all the fits clearly demonstrates that the γ-symmetry quadrupolar ordering, which occurs at 5 K, is of ferroquadrupolar type, the spin system remaining under-critical at any temperature. Among the rare-earth intermetallics, $TmAg_2$ then allows one a perfect comparison with the tetragonal rare-earth insulators RXO_4, which constitute archetypes of the Jahn-Teller couplings.

The properties resulting from the complex balance between spin and quadrupolar interactions are analyzed within the tetragonal symmetry using a complete susceptibility formalism. The latter allows us to separately determine the different couplings, step by step, symmetry by symmetry. The starting step is a thorough knowledge of the five CEF parameters deduced from inelastic neutron-scattering spectra and the characteristic behaviors of the magnetic susceptibility in $TmAg_2$ itself, but also in isomorphous compounds. It is then possible to take into account in the analysis the specific features of all the CEF levels, in particular the effects driven by off-diagonal matrix elements between CEF levels.

The three α-, γ-, and δ-symmetry-lowering modes have been studied with regard to both the magnetoelasticity and the quadrupolar pair interactions. The α mode, which keeps the tetragonal symmetry, and the orthorhombic δ mode play minor roles, and are overwhelmed by the γ-symmetry mode. Thus the determinations of the B and K coefficients for these two modes are delicate and will be presented in a forthcoming paper, based on magnetostriction and ultrasonic velocity measurements.

Concerning the γ symmetry, the determination of the quadrupolar coefficients is monolithic. The parastriction, the C_{11}-C_{12} ultrasonic mode and the third-order magnetic susceptibility, are described with a unique value $G^{\gamma}=18\pm1$ mK for the total quadrupolar coefficient. This value closely describes the $\langle O_2^2 \rangle$ quadrupolar ordering, which occurs at $T_Q=5$ K, through a second-order transition. The parastriction and the softening of C_{11}-C_{12} allow us to determine the respective contributions of the magnetoelastic coupling and of the pair interactions: $B^{\gamma}=-31\pm2$ K $[(B^{\gamma})^2/C_0^{\gamma}=7.0\pm0.2$ mK] and $K^{\gamma}=10\pm1$ mK.

The quadrupolar ordering is then driven by the pair interactions. K^{γ} by itself would give an ordering temperature $T_Q=2.5$ K. The spontaneous strain, $\varepsilon_{\gamma}=-3.5\times10^{-3}$ at 1.6 K,[24] is the best evidence of this ordering through the magnetoelastic coupling, which ob-

viously reinforces the K^{γ} effect and moves the T_Q temperature up to 5 K. The ratio $K^{\gamma}/[(B^{\gamma})^2/C_0^{\gamma}]=1.4$ is reminiscent of values observed in TmZn (Ref. 4) and TmCd (Ref. 9) cubic intermetallics. In these latter systems, the pair interactions have been shown to be mediated by the conduction electrons rather than by phonons.[1] The same analysis seems to be valid in $TmAg_2$. This situation is then opposite to that for insulators, for which a ratio $K^{\gamma}/(B^{\gamma})^2/C_0^{\gamma}=-\frac{1}{3}$ is observed. In insulators, the magnetoelastic coupling drives a Jahn-Teller transition at a temperature, which would be slightly higher in the absence of the negative K^{γ} term.

The remarkable relevancy of the mean-field approximation to the determination of the quadrupolar ordering is surprising. It has also been observed in cubic intermetallics. In these systems, the first-order character of the transition may be expected to hide fluctuations in the high-temperature range. This explanation is no longer valid for the second-order transition in $TmAg_2$. We plan to try to determine critical exponents in order to check more deeply the validity of this MFA hypothesis. The study of the dispersion curves in the orthorhombic and tetragonal phases will be possible as soon as a large enough single crystal has been grown.

ACKNOWLEDGMENTS

It is a great pleasure to thank Dr. A. Huxley for a critical reading of the manuscript. The Laboratoire Louis Néel is Unité Associée à l'Université Joseph-Fourier, Grenoble.

[1]P. Morin and D. Schmitt, in *Ferromagnetic Materials* edited by K. H. J. Buschow and E. P. Wohlfarth (North-Holland, Amsterdam, 1990), Vol. 5, p. 1.
[2]M. Kataoka and J. Kanamori, J. Phys. Soc. Jpn. **32**, 113 (1972).
[3]G. A. Gehring and K. A. Gehring, Rep. Prog. Phys. **38**, 1 (1975).
[4]R. L. Melcher, in *Physical Acoustics,* edited by W. P. Mason and R. N. Thurston (Academic, New York, 1976), Vol. XII.
[5]D. Schmitt, P. Morin, and J. Pierre, J. Magn. Magn. Mater. **8**, 249 (1978).
[6]A. V. Andreev, A. V. Deryagin, and S. M. Zadworkin, Zh. Eksp. Teor. Fiz. [Sov. Phys. JETP **58**, 566 (1983)].
[7]V. M. T. S. Barthem, D. Gignoux, D. Schmitt, and G. Creuzet, J. Magn. Magn. Mater. **78**, 56 (1989).
[8]M. Atojii, J. Chem. Phys. **51**, 3877 (1969); **51**, 3882 (1969); **57**, 851 (1972).
[9]E. Bucher, K. Andres, J. M. Maita, A. S. Cooper, and L. D. Longinotti, J. Phys. (Paris) Colloq. **32**, C1-114 (1971).
[10]M. Atojii, J. Chem. Phys. **52**, 6433 (1970).
[11]P. Morin, J. Rouchy, and D. Schmitt, Phys. Rev. B **37**, 5401 (1988).
[12]K. W. H. Stevens, Proc. Phys. Soc. London, Sect. A **65**, 209 (1952).
[13]D. Gignoux, P. Morin, and D. Schmitt, J. Magn. Magn. Mater. **102**, 33 (1991).
[14]E. du Trémolet de Lacheisserie, Ann. Phys. **5**, 267 (1970).
[15]P. Morin, D. Schmitt, and E. du Trémolet de Lacheisserie, Phys. Rev. B **21**, 1742 (1980).
[16]A. E. Dwight, J. W. Downey, and R. A. Conner, Acta Crystallogr. **22**, 745 (1967).
[17]P. Morin and J. Blanco, J. Magn. Magn. Mater. **119**, 59 (1993).
[18]G. F. Koster, J. O. Dimmock, R. G. Wheeler, and H. Statz, in *Properties of the Thirty-Two Points Groups,* edited by J. A. Stratton (MIT Press, Cambridge, 1963).
[19]P. Boutron, Phys. Rev. B **7**, 3226 (1973).
[20]D. Schmitt, J. Phys. F **9**, 1745 (1979).
[21]P. Morin, in *Magnetic Properties of Metals,* edited by H. P. J. Wijn, Landolt-Börnstein New Series, Vol. 19.e.2 (Springer, Berlin, 1989), p. 1.
[22]R. R. Birss, in *Symmetry and Magnetism,* edited by E. P. Wohlfarth (North-Holland, Amsterdam, 1964).
[23]E. du Trémolet de Lacheisserie, Rev. Phys. Appl. **10**, 169 (1975).
[24]P. Morin and J. Rouchy (unpublished).